

# Beam characterization at NSRL for radiobiological experiments – phase 1

---

L. Burigo<sup>a,b,1</sup> T. Gehrke<sup>a,b</sup> O. Jäkel<sup>a,b,c</sup> M. Sivertz<sup>d</sup> T. Olsen<sup>d</sup> A. Rusek<sup>d</sup>  
C. Obcemea<sup>e</sup> and S. Greilich<sup>a,b,2</sup>

<sup>a</sup>German Cancer Research Center (DKFZ), Heidelberg, Germany

<sup>b</sup>National Center for Radiation Research in Oncology (NCRO), Heidelberg Institute for Radiation Oncology (HIRO) Heidelberg, Germany

<sup>c</sup>Heidelberg Ion-Beam Therapy Centre (HIT) Heidelberg, Germany

<sup>d</sup>NASA Space Radiation Laboratory, Brookhaven National Laboratory, Upton, New York, USA

<sup>e</sup>Radiation Research Program, Division of Cancer Treatment and Diagnosis, National Cancer Institute, National Institutes of Health, Bethesda, Maryland, USA

E-mail: [L.Burigo@dkfz-heidelberg.de](mailto:L.Burigo@dkfz-heidelberg.de)

**ABSTRACT:** An experimental campaign with the aim to perform an additional, independent dosimetric characterization of the beams of protons, helium and carbon ions at the NASA Space Radiation Laboratory for radiobiological experiments was undertaken by the request and with the support from the National Cancer Institute, US. In this initial phase, the goals were to obtain a first assessment of the stability and reproducibility of the ion beams, including analysis of spatial homogeneity and evaluation of ion beam contamination in order to facilitate the design of further experimental campaigns for characterization of the beam for radiobiological experiments. Measurements included reference dosimetry with comparison of in-house and external ionization chambers and electrometers, lateral dose profile measurements in air, depth dose profile in a water tank, evaluation of water equivalent thickness of a HDPE binary range shifter and estimation of impurities of the investigated charged particle beams. The experiments and results are presented.

**KEYWORDS:** Dosimetry concepts and apparatus, Detector alignment and calibration methods, Radiotherapy concepts, Instrumentation for heavy-ion therapy

---

<sup>1</sup>Corresponding author.

<sup>2</sup>Current address: Berthold Technologies GmbH & Co. KG, Calmbacher Straße 22, 75323 Bad Wildbad, Germany

---

## Contents

<b>1</b>	<b>Background</b>	<b>1</b>
<b>2</b>	<b>Material and Methods</b>	<b>2</b>
2.1	Ion beams	2
2.2	Equipment	3
2.3	Reference dosimetry	3
2.4	Dose profiles	3
2.5	WET determination of binary range shifter layers	6
2.6	Beam impurity	7
<b>3</b>	<b>Results</b>	<b>8</b>
3.1	Reference dosimetry	8
3.2	Lateral-dose profiles	12
3.3	Depth-dose profiles and range in water	13
3.4	WET of HDPE layers	14
3.5	Purity of the helium-ion beam	16
<b>4</b>	<b>Conclusions</b>	<b>18</b>

---

## 1 Background

The increasing number of ion beam therapy facilities worldwide<sup>1</sup> and their encouraging clinical results have led to a growing interest in research projects connected to ion beam radiotherapy in the US. Consequently, the NASA Space Radiation Laboratory (NSRL)[1, 2] at Brookhaven National Laboratory as the only ion beam research facility in the US is increasingly used for basic radiobiological research in the context of light ion beam therapy[3]. Since the results of radiobiological experiments with light ion beams may be used to generate a rationale for the clinical use of light ions beams in the US, it is of great importance to ensure the validity of the generated data. Accurate knowledge of beam properties and dosimetry parameters is key for the validity of these studies and to enable intercomparison[4]. To support current procedures, the National Cancer Institute launched a program for an independent characterization of the ion beam at NSRL for the purpose of radiobiological experiments. As part of this initiative, a team of researchers from the German Cancer Research Center (DKFZ) conducted a series of measurements from February 28, 2019 to March 1, 2019 using equipment complementary to devices at NSRL. These first phase experiments focused on reference dosimetry, beam shape and potential contamination of the ion beams, as these are considered key factors for accurate dosimetry.

---

<sup>1</sup>Current facilities in operation and patient statistics as reported by the Particle Therapy Co-Operative Group is available at <https://www.ptcog.ch/>

## 18 2 Material and Methods

### 19 2.1 Ion beams

20 NSRL provides ion beams from protons to gold nuclei, which are extracted from the Booster  
21 synchrotron of Brookhaven National Laboratory with energies from 50 to 1,500 MeV/n (up  
22 to 2,500 MeV for protons). For radiation therapy-related research, the species of interest  
23 are protons to neon ions with energies up to around 500 MeV/n available at dose rates  
24 up to around 4 Gy/min (depending on ion species and field size). The sources used to  
25 produce the ions are either a LINAC (for protons) or the Electron Beam Ion Source (EBIS)  
26 equipped with gas sources like helium and a laser ion source for any type of solid target,  
27 which can quickly change ion species within a few pulses. Ion beams produced from the  
28 laser ion source are especially susceptible to contamination from other ions with the same  
29 charge to mass ratio as the primary ion. Furthermore, traces of atmospheric gases like  
30 nitrogen, oxygen, and carbon are almost always present in the source vacuum chamber and  
31 are common contaminants. When accelerating helium it is also not unusual to find neon  
32 contamination in the gas cylinder supplying the helium gas to the source chamber.

33 The ion beams at NSRL are delivered by a horizontal beamline through a set of mag-  
34 netic dipole, quadrupole and octupole lenses, which control the size and shape of the beam  
35 to match the desired radiation field. A large tungsten collimator may be used to control the  
36 overall field size and additional small collimators may be inserted, if a small pencil-beam is  
37 needed. The beam energy can be actively changed by modifying the synchrotron settings,  
38 or passively with the use of a binary range shifter placed in the beamline inside the exper-  
39 imental room. The binary range shifter is made from high density polyethylene (HDPE).  
40 Additionally, if an energy modulation (spread out Bragg beam) is needed, dedicated mod-  
41 ulator wheels may be inserted. In the set of experiments below, the field size was tuned to  
42 irradiate a  $20 \times 20 \text{ cm}^2$  area which is qualitatively monitored with respect to homogeneous  
43 fluence using a digital beam imager (DBI). The DBI consists of a luminescence screen which  
44 is read out by an optical system and a CCD camera. The DBI is inserted in the beam line  
45 just behind the position where measurements are taken, and displays beam uniformity with  
46 a typical homogeneity of 3% throughout the inner part of the field.

47 In this first set of investigations, mainly mono-energetic beams were used. One of  
48 the available beam modulator wheels, which was built for a prior experiment was also  
49 investigated, but not expected to provide a very homogeneous dose in the SOBP. The  
50 following ions beams with approximately 20 cm range in water were used in the experiments:

- 51 • 173 MeV protons,
- 52 • 173 MeV/n helium ions,
- 53 • 326 MeV/n carbon ions.

54 When an ion beam is requested, a certain number of ions is also selected, which is then  
55 controlled by a first large area monitor chamber (usually QC3 chamber, see Table 1). This  
56 chamber reading may be used as a reference signal to control the beam and may be used

57 to normalize the results from different experiments. The monitor chamber is routinely cali-  
58 brated against a NIST calibrated ionization chamber prior to each run (usually “EGG600”,  
59 see Table 1).

## 60 **2.2 Equipment**

61 The laboratory equipment used in the experiments is listed in Table 1. For the reference  
62 dosimetry experiments, Far West ionization chambers currently used at NSRL and two  
63 Farmer chambers were used in combination with 3 different readout electrometers. Lateral  
64 dose profiles in air were measured with a small-sized cylindrical PinPoint chamber, while  
65 depth-dose profiles in water were obtained using a plane parallel Markus chamber. In both  
66 profile measurements, the field chambers were fixed to a motorized arm in a phantom tank  
67 allowing accurate positioning of the chamber in the field. Last, a set of 3 Timepix silicon  
68 pixel detectors were mounted as a telescope device allowing identification of individual ion  
69 tracks for evaluation of beam contaminants.

70 All equipment from DKFZ was calibrated and certified in December 2018 by PTW  
71 (Freiburg, Germany), to ensure correct functioning and traceability of the measured doses  
72 to the German national primary standard for dose, which is also the basis for ion beam  
73 radiotherapy in Germany. The same type of equipment is used routinely at the Heidelberg  
74 Ion-Beam Therapy Center in daily clinical practice for ion beam dosimetry.

## 75 **2.3 Reference dosimetry**

76 Reference dosimetry measurements were performed to compare the response of the ion-  
77 ization chambers used at NSRL, Far West Technology “EGG” (S/N 600 and S/N 908),  
78 against the calibrated ionization chambers PTW 30013 Farmer. To account for possible  
79 impact of the readout, different readout devices were used, namely the 2 recycling integra-  
80 tors from NSRL (“EGG1” and “EGG2”) and the PTW UNIDOS Electrometer T10021. In  
81 all the experiments, the chamber “EGG” (S/N 600) and the recycling integrator “EGG1”  
82 were used as reference. Measurements were performed for 173 MeV proton and 326 MeV/n  
83 carbon ion beams. The chambers were mounted with build-up cap and placed at the same  
84 distance from the beam window which correspond to the position typically used for the  
85 radiobiological experiments (see Figure 1). A second set-up made use of the PTW 30013  
86 Farmer chambers placed in a RW3 Farmer chamber plate with the “EGG” chambers lo-  
87 cated directly upstream of the plate. The readout from the UNIDOS<sup>webline</sup> electrometer  
88 was accessed remotely using the corresponding VNC viewer. In total, 298 measurements  
89 from 145 irradiations in 16 runs were performed, accounting for 13 out of the 24 possible  
90 permutations of chamber/readout/beam (see Figure 2). Measurements were performed for  
91 requested doses of 0.1 Gy (carbon-ion beam) and 0.2 Gy (proton beam).

## 92 **2.4 Dose profiles**

93 Dose profiles were performed using a MP3 phantom tank mounted with a TBA control unit  
94 for remote positioning of the field chamber mounted inside the tank. A reference chamber  
95 was mounted upstream of the tank and positioned in such a way to not shadow the field  
96 chamber. The readout data were remotely collected using the tbaScan application from

**Table 1.** Laboratory equipment from NSRL and complementary equipment from DKFZ used in the experiments.

<b>Equipment</b>	<b>Comments</b>
<b>Equipment from NSRL</b>	
Far West Technology “EGG” Ionization Chamber	S/N: 600, NIST calibrated ionization chamber, 1 cm <sup>3</sup> nominal sensitive volume, used as reference chamber in the experiments for relative comparisons, in the following denominated as “EGG600”
Far West Technology “EGG” Ionization Chamber	S/N: 908, 1 cm <sup>3</sup> nominal sensitive volume, in the following denominated as “EGG908”
“EGG1” Recycling Integrator	Used as reference electrometer in the experiments for relative comparisons
“EGG2” Recycling Integrator	
Monitor chamber QC1	Large planar ion chamber located approximately 10 cm from vacuum window. Used in combination with QC3 and binary range shifter to measure Bragg curves
Monitor chamber QC3	QC3 chamber used to cut-off the irradiation located approximately 500 cm from vacuum window
Binary Range Shifter	Set of remotely-driven HDPE layers with thickness varying from 0.25 mm to 128 mm
Luminescence Screen	Scintillator camera
Beam Modulator Wheel	Custom made for modulation of 1.2 cm SOBP for carbon-ion beam
Collimators	Blocks of tungsten
<b>Equipment from DKFZ</b>	
2 PTW Farmer-type Ionization Chambers	S/N: TM30013-03641 and TM30013-001583, 0.6 cm <sup>3</sup> nominal sensitive volume
2 PTW Markus-type Ionization Chambers	S/N: TM34045-0318 and TM34045-0615, 0.02 cm <sup>3</sup> nominal sensitive volume
1 PTW Pinpoint Ionization Chamber	S/N: TM31014-0015, 0.015 cm <sup>3</sup> nominal sensitive volume
PTW TANDEM Electrometer	S/N: T10011-10365
PTW UNIDOS <sup>webline</sup> Electrometer	S/N: T10021-0269
PTW MP3 phantom tank	Remote-controlled 3D acrylic water tank with 20 mm thick walls and a scanning range of 60×50×40.8 cm <sup>3</sup> .
PTW TBA Control Unit	S/N: T41013-0623
PTW TRUFIX base set	S/N: 981150
PTW RW3 slab phantom	Farmer chamber slab 29672/U19
PTW MEPHYSTO mc2 software	Version 1.8.0
3 Timepix detectors	Silicon pixel detectors with 55 μm pixel pitch, 300 μm sensor thickness, first generation; S/N: SPN3-3G1 (E07-W167), SPN3-3F6 (C07-W167), SPN3-3E4 (C08-W167)
1 FITPIX read-out interface	For read-out of Timepix detectors. S/N: FITPIX 0022
Pixet software	For data acquisition and steering of Timepix detectors. Version 1.4.7

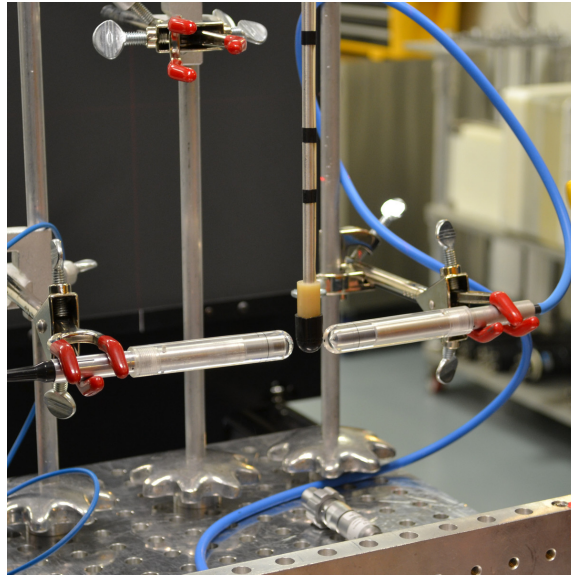


**Figure 1.** Set-up with the vertically-positioned reference chamber “EGG600” and two horizontally-positioned Farmer chambers.

Number of runs per combination

		C, 326 MeV/u			
Readout	UNIDOS	2		7	5
	EGG2	3			3
	EGG1	5	1	1	2
		p, 173 MeV			
UNIDOS				1	1
EGG2	1				
EGG1	1				
		EGG600	EGG908	F3641	F1583
		Chamber			

**Figure 2.** Number of runs per combination of chamber and readout device for carbon-ion beam (upper panel) and proton beam (lower panel).

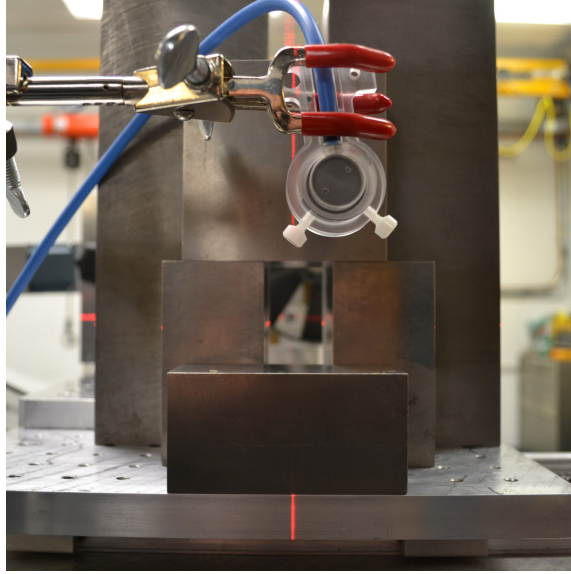


**Figure 3.** Set-up for measurements of SOBP. The reference TM34045 Markus chamber with build-up cap is displayed upstream of the collimator. The modulator wheel can be seen through the gap of the collimation.

97 MEPHYSTO software. The electrometer was reset before the data collection in every run.  
 98 Measurements were taken on time basis with the time being equal to an integer multiple of  
 99 the cycle time of the accelerator. Lateral-dose profiles in air were measured using a TM34045  
 100 Markus chamber (S/N 0318) as reference chamber and a TM31014 PinPoint chamber (S/N  
 101 0015) as field chamber. Depth-dose profile measurements were performed by filling the  
 102 MP3 phantom tank with demineralized water and using 2 TM34045 Markus chambers (S/N  
 103 0318 used as reference chamber, S/N 0615 used as field chamber). Measurements were also  
 104 performed for a SOBP using a modulator wheel in which case the beam was collimated  
 105 downstream of the reference chamber. The beam modulator wheel and collimators were  
 106 positioned in such a way that the modulated beam was aligned with the field chamber in  
 107 the beam-eye-view (cf. Figure 3).

## 108 2.5 WET determination of binary range shifter layers

109 Since the binary range shifter mounted in the beamline is typically used at NSRL to pas-  
 110 sively change the energy of the ion beam or to measure depth-dose curves for range esti-  
 111 mation, it is relevant to evaluate the water-equivalent thickness (WET) of the layers. The  
 112  $WET_i$  of each layer  $i$  was estimated by the changes of  $R_{80}$ <sup>2</sup> range in water as follows

$$WET_i = R_{80,ref} - R_{80,i}$$

113 where  $R_{80,ref}$  corresponds to the range of a 326 MeV/n carbon ion beam in water, and  $R_{80,i}$   
 114 the range after traversing the layer  $i$ . The estimation of WET could also be used to evaluate

---

<sup>2</sup> $R_{80}$  is characterized by the depth at the distal dose fall-off where the dose drops to 80% of the maximum dose level.

115 the water-equivalent path length (WEPL) in HDPE as follows

$$\text{WEPL} = \frac{(R_{80,\text{ref}} - R_{80})}{\text{layer thickness}}.$$

## 116 **2.6 Beam impurity**

117 To have an initial estimation of the purity of ion beams at NSRL, analysis of contamina-  
118 tion for a 173 MeV/n helium-ion beam was performed using a set of Timepix silicon pixel  
119 detectors. The aim of this study was to determine if other ion types heavier than helium  
120 ions are present in the requested helium-ion beam, and if so, the relative amount of the  
121 contaminants. The presence of lighter fragments produced inevitably by nuclear fragmen-  
122 tation were not investigated, as this process is well known. To differentiate between ion  
123 types, their energy deposition in the 300- $\mu\text{m}$ -thick silicon layer of the Timepix detectors  
124 was measured. Since the energy deposition depends on the squared charge number of the  
125 impinging ion<sup>3</sup> and the traversing ions are expected to have approximately the same specific  
126 energy, well-differentiated energy depositions connected to different ion types are expected.

127 Post-processing of the data has to be carried out to identify and remove spurious signals  
128 that are neither caused by incident primary helium ions nor by contamination ions (e.g.  
129 signals caused by recoil nuclei in silicon or by overlapping/integrated signals of two or more  
130 ions). This is necessary to allow for an unbiased quantitative analysis of beam purity. To  
131 facilitate this procedure, not only the energy deposition of single ions in one detector was  
132 measured, but track identification was performed by using a telescope consisting of three  
133 synchronized Timepix detectors. The set of detectors provide for each signal a spatial  
134 resolution better than the pixel pitch of 55  $\mu\text{m}$  of the detector. The first detector was used  
135 to measure the energy deposition, while the last two detectors were used to measure the  
136 arrival time of the impinging particles. The time stamps on the last two detectors were used  
137 to identify coincident hits, and these coincidences were connected to the measured energy  
138 deposition by back-projection of the corresponding tracks onto the energy detector. In this  
139 way, signals due to recoils and other background which are not observed in all three detector  
140 layers, as well as overlapping signals from multiple tracks, can be identified and removed.  
141 The next step in the analysis is the generation of two-dimensional (2D) histograms of  
142 energy deposition in detector 1 on the first axis and the corresponding cluster size (defined  
143 as number of adjacent hit pixels) on the second axis. Since the cluster size is an additional  
144 parameter that helps to classify different signals, the final differentiation between signals  
145 caused by primary helium ions and signals caused by other ion types due to beam impurities  
146 is based on the 2D histogram and not only on the energy deposition information.

---

<sup>3</sup>In general, the energy deposition of an ion traversing a material depends on several material properties as well as the charge and velocity of the incident ion. By assuming that different ion types (primary and impurities) are travelling at the same velocity (same energy per nucleon), the relative energy deposition in the silicon layer depends solely on the ration of the squared charge of the ions.

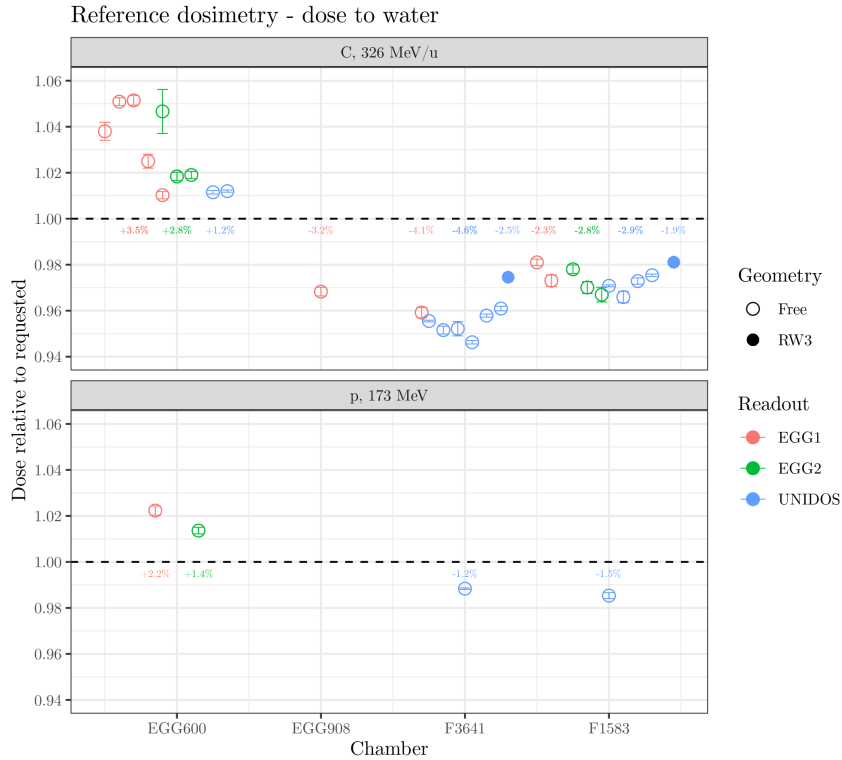


**Figure 4.** Mean dose response data over different runs for the “EGG” ionization chambers S/N 600 (EGG600) and S/N 908 (EGG908) and Farmer chambers S/N TM30013-03641 (F3641) and S/N TM30013-001583 (F1583). Colours are used to differentiate the readout device. Filled circles represent the measurements with the Farmer chamber placed inside the RW3 slab phantom.

### 147 3 Results

#### 148 3.1 Reference dosimetry

149 The dose response in the reference dosimetry measurements was evaluated with respect  
 150 to the influence of the chamber type, readout device, ion type and set-up geometry. The  
 151 response of the monitor chamber (employed to cut-off the irradiation) was used to evaluate  
 152 the beam stability. The measured dose shows an average deviation of +0.02% and -0.02%  
 153 from the requested dose for protons and carbon ions, respectively, with a relative variation of  
 154 0.09% and 0.03% (1 standard deviation). The ionization chamber-specific response averaged  
 155 over different irradiations is presented in Figure 4 for the irradiation with proton and carbon-  
 156 ion beams using different combinations of the readout devices. In the following, except when  
 157 explicitly stated otherwise, the results obtained using the RW3 slab phantom are excluded  
 158 from the analysis to avoid introducing a bias in the response with the Farmer chambers.

159 Figure 5 shows the influence of the chamber type. The dose response of the chamber  
 160 EGG600 was, on average, 2.5% higher than the requested dose. The dose response of  
 161 the chambers EGG908, F3641 and F1583 were lower than the requested dose by 3.2%,  
 162 3.7% and 2.5%, respectively. Approximately 5–6% difference between chamber EGG600  
 163 and the other chambers was observed. Tukey multiple pairwise-comparisons was used to

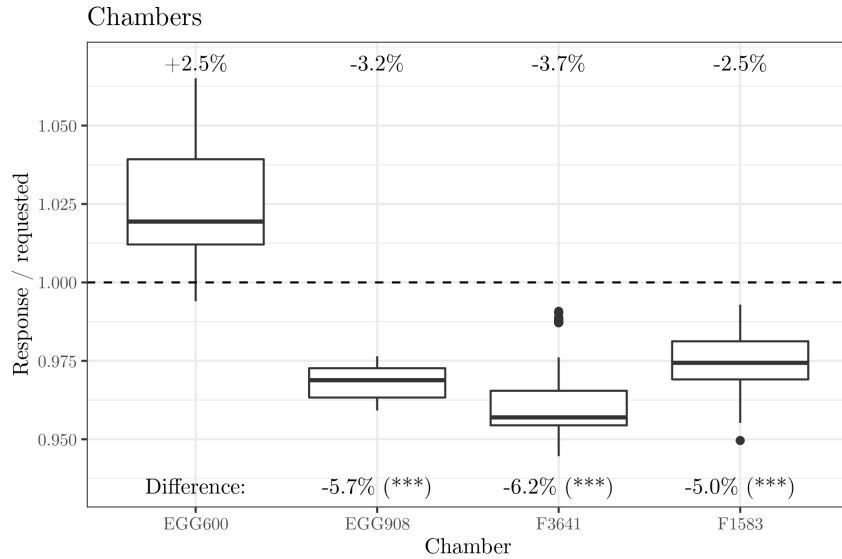


**Figure 5.** Influence of chamber type on the chamber dose response. Values on the top indicate the deviation w.r.t. the requested dose, while values on the bottom evaluate the significance of the difference in the results w.r.t. the results obtained with the reference chamber EGG600.

164 evaluate the significance of the differences. Except for the pair comparison between EGG908  
 165 and each of the Farmer chambers, all other differences among the chambers are mutually  
 166 significant.

167 Figure 6 shows the influence of the readout device on the response of the ionization  
 168 chambers. The dose response obtained with the readout EGG1 is, on average, 1.3% higher  
 169 than the requested dose. In contrast, the other two readouts show average dose response  
 170 lower than the requested dose, -0.5% for EGG2, and -2.5% for UNIDOS. Mutually sig-  
 171 nificant differences in the response depending on the readout device were observed. The  
 172 response with UNIDOS is on average approximately 4% lower than the response using EGG1.  
 173 Differences between EGG1 and EGG2 are smaller (1.8%).

174 The influence of the readout device segmented per chamber type is shown in Figure 7.  
 175 The results show that the main effect observed for the dependence of the chamber response  
 176 on the readout device is driven by the response of the chamber EGG600. In contrast, the  
 177 response of the Farmer ionization chambers is substantially less sensitive to the specific  
 178 readout device used.

179 Figure 8 shows the influence of the beam on the chamber response for 4 specific com-  
 180 binations of chamber and readout. Significant differences between the response to proton  
 181 and carbon-ion beams are observed. The response to protons is smaller for the EGG600  
 182 chamber with respect to the response to carbon ions, while the opposite effect is observed  
 183 for the Farmer ionization chambers.

184 Figure 9 shows the influence of the geometry set-up on the response of the Farmer  
 185 ionization chambers, i.e., free in air, or mounted inside the RW3 slab phantom. As expected,  
 186 the variability of the chamber response is substantially reduced when the chamber is placed

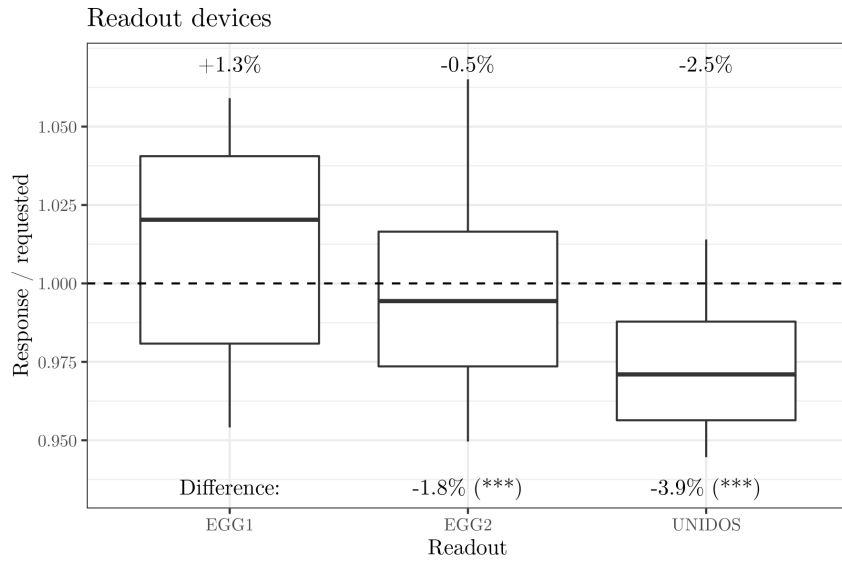


**Figure 6.** Influence of readout device on the chamber dose response. Values on the top indicate the deviation w.r.t. the requested dose, while values on the bottom evaluate the significance of the difference in the results w.r.t. the results obtained with the reference readout EGG1.

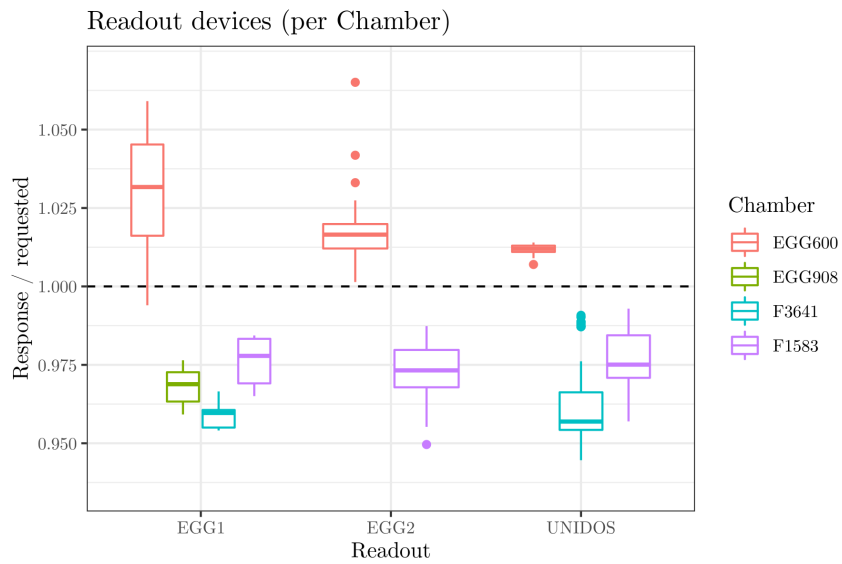


**Figure 7.** Influence of readout device on the chamber dose response segmented per chamber type.

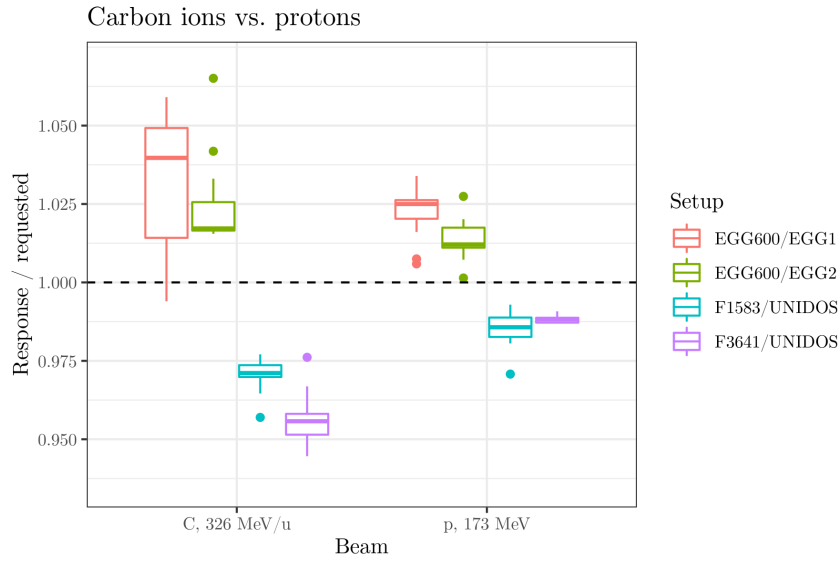


**Figure 8.** Influence of ion beam on the chamber response for 4 combinations of chamber and readout device.

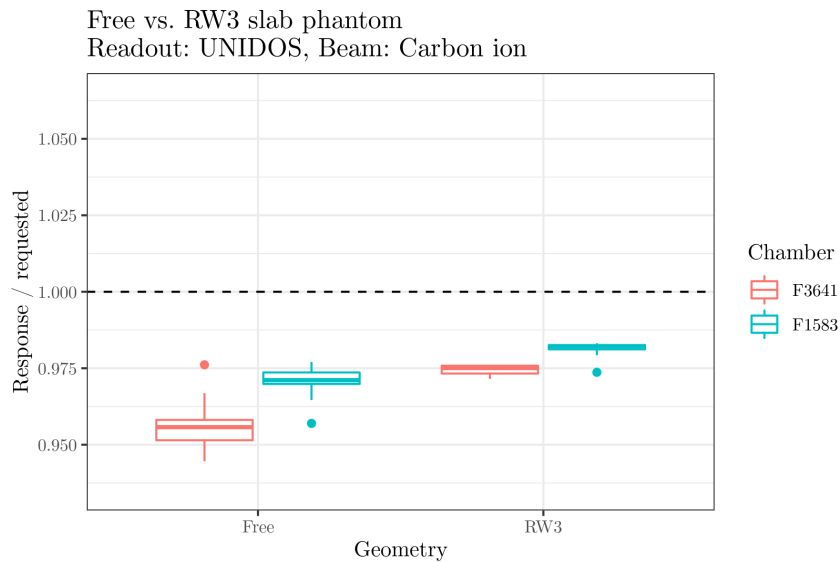


**Figure 9.** Influence of geometry on the dose response of the Farmer chambers using the UNIDOS readout for irradiation with carbon ion beam.

187 inside the RW3 slab phantom, followed by an increase of the response which is in line with  
 188 the increase of stopping power due to the increase of material in the beam path.

189 The variability of the chamber response were evaluated with respect to chamber type  
 190 and readout used. In each case, the variability was first corrected for the observed linear  
 191 trend of the response as a function of time of irradiation for a given run. No significant  
 192 differences in variability were observed due to the chamber type (see Figure 10). Regarding  
 193 the impact of the readout device, UNIDOS shows significantly (3 fold) less variability across

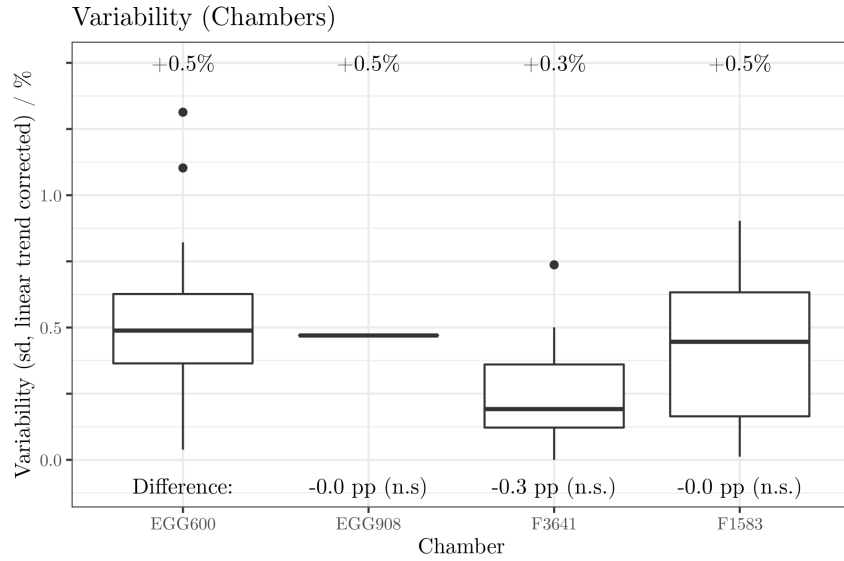


**Figure 10.** Influence of chamber type on response variability. The reponse variability is corrected by the linear trend of the response as a function of time of irradiation.

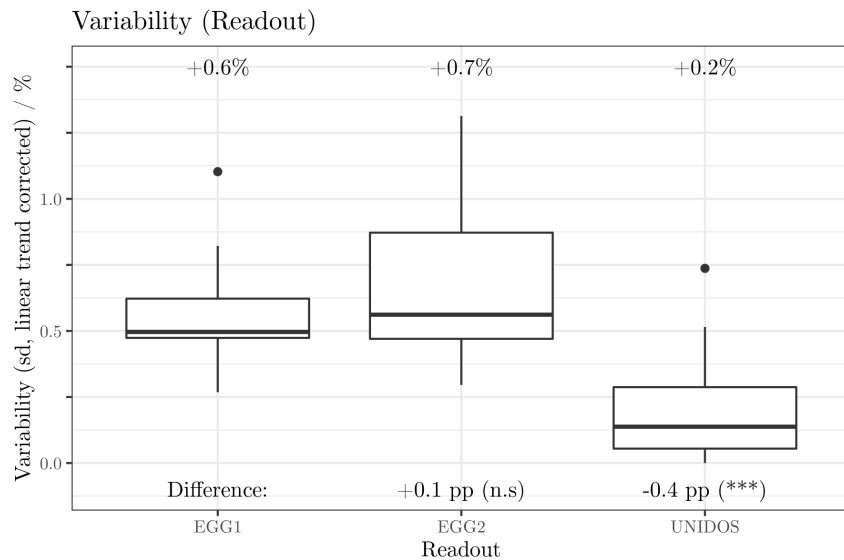


**Figure 11.** Influence of readout type on response variability. The reponse variability is corrected by the linear trend of the response as a function of time of irradiation.

194 all chambers in comparison to the readout devices EGG1 and EGG2 (see Figure 11).

### 195 3.2 Lateral-dose profiles

196 Field homogeneity was evaluated by means of lateral dose profile measurements in a  $10 \times 10 \text{ cm}^2$   
 197 central region. Figure 12 shows the lateral-dose profiles for 173 MeV proton and 326 MeV/n  
 198 carbon-ion beams in the horizontal and vertical direction normalized to the response at  
 199 the center of the field. The variation (1 standard deviation) of the chamber response for

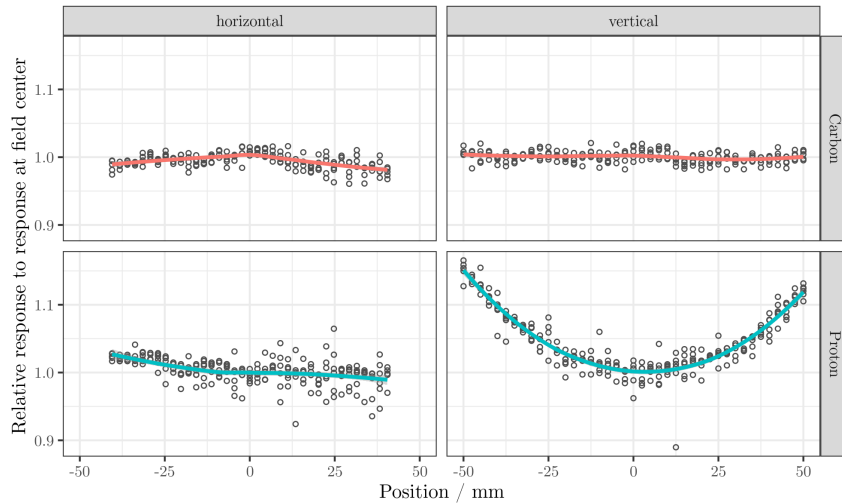


**Figure 12.** Chamber response relative to the response at the center of the field for 173 MeV proton and 326 MeV/n carbon-ion beams measured in horizontal and vertical direction.

200 protons is 1.9% and 4.4% in the horizontal and vertical direction, respectively. For carbon  
 201 ions, the variation is significantly lower corresponding to 1.1% and 0.8% in the horizontal  
 202 and vertical directions, respectively. Despite the large uncertainty in the chamber response,  
 203 a significant ( $p < 0.05$ ) underlying dependence of the chamber response on the position in  
 204 the field was observed for all cases. In particular, a large increase of dose towards the edge  
 205 of the field (up to 15% higher at 50 mm distance from the center of the field) was observed  
 206 for the proton beam in the vertical direction.

### 207 3.3 Depth-dose profiles and range in water

208 Figure 13 shows the measured depth-dose profiles for the 173 MeV proton beam. It should  
 209 be emphasized that the beam settings are manually adjusted in contrast to pre-defined  
 210 settings used in clinical facilities. Therefore, it is relevant to evaluate the reproducibility of  
 211 the measurements. The results could be well reproduced in the two consecutive days with  
 212 range in water of  $R_{80} = 207.2 \pm 0.5$  mm in water (i.e., only 0.2% variation of range).

213 Figure 14 shows the measured depth-dose profiles for the 173 MeV/n helium-ion beam.  
 214 Differently from the proton beam, the helium-ion beam was not stable compromising  
 215 the measurements. The Bragg curve could only be measured in one day of the exper-  
 216 imental campaign. The 173 MeV/n helium-ion beam was observed to have a range of  
 217  $R_{80} = 207.4 \pm 0.6$  mm in water.

218 Figure 15 shows the measured depth-dose profiles for 326 MeV/n carbon-ion beam. The  
 219 range in water was observed to be  $R_{80} = 201.2 \pm 0.2$  mm indicating a variation of  $R_{80}$  of  
 220 only 0.1% in different days.

221 Figure 16 shows the depth-dose profile obtained by modulation of 217 MeV/n and  
 222 326 MeV/n carbon-ion beam using an in-house-machined modulator wheel. A relatively  
 223 flat 25 mm-wide spread-out Bragg peak is achieved with the modulation indicating the  
 224 capability of producing SOBP beams necessary for radiobiological experiments.

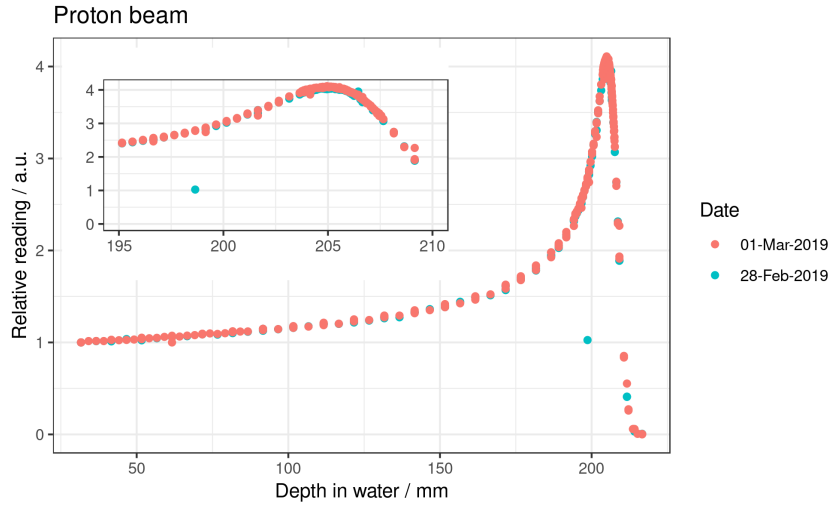


Figure 13. Depth-dose profile in water for the 173 MeV proton beam.

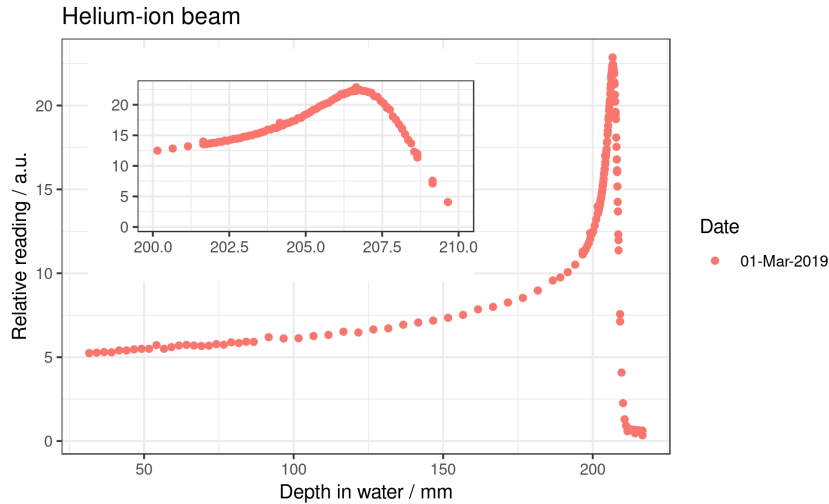
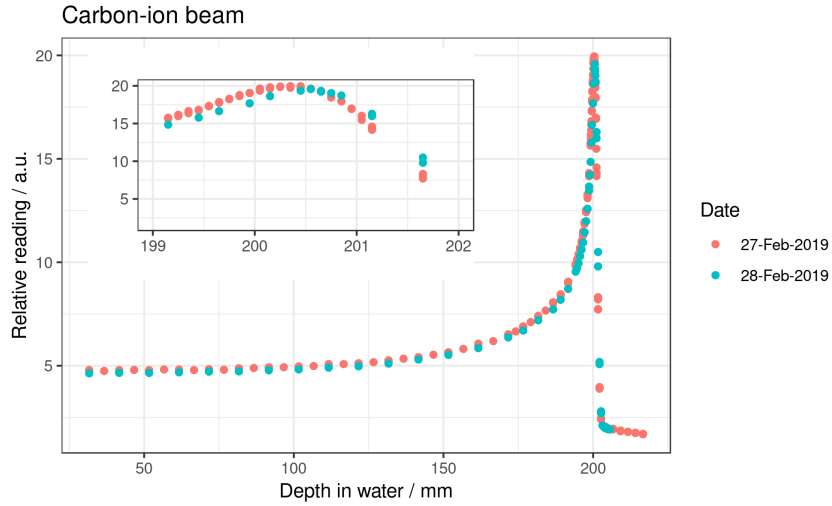


Figure 14. Depth-dose profile in water for 173 MeV/n helium ion beam.

### 225 3.4 WET of HDPE layers

226 The estimated WET of the individual HDPE layers of the binary range shifter is shown in  
 227 Table 2. Unexpected small WET was observed for the thin layers indicating a WEPL of  
 228 HDPE smaller than unity. Since the uncertainty in the WET as well as in the machined  
 229 thickness of the HDPE layers are larger for the thin layers, only layers with thickness  
 230  $t \geq 8$  mm were selected to evaluate the WEPL of HDPE. This approach resulted in a  
 231 mean value for the WEPL of the HDPE used in the range shifter of 1.025.

232 Figure 17 shows the depth-dose profile measured in water with the Markus ionization  
 233 chamber and the water-equivalent Bragg profiles obtained for carbon-ion beam using the  
 234 binary range shifter and the two large planar ion chambers QC1 and QC3.



**Figure 15.** Depth-dose profile in water for 326 MeV/n carbon ion beam.

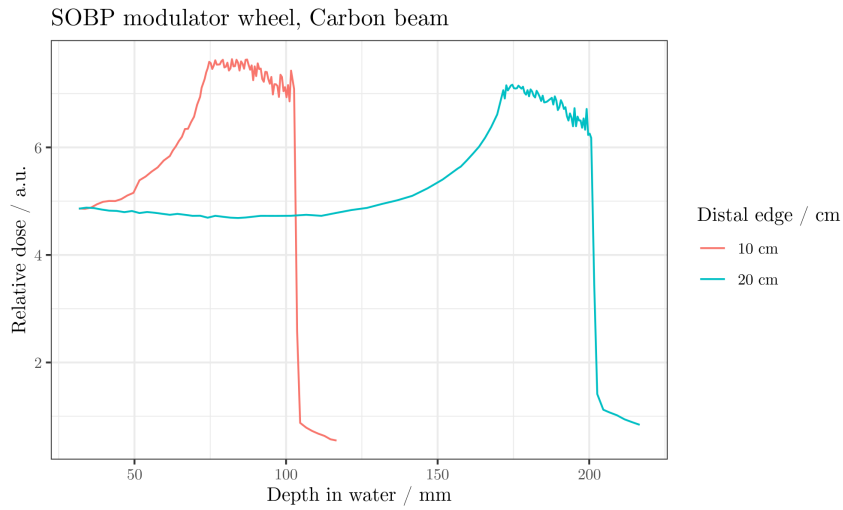


**Figure 16.** Depth-dose profile in water for 217 MeV/n and 326 MeV/n carbon-ion beam with an in-house-machined modulator wheel.

**Table 2.** Thickness of binary range shifter layers, range in water ( $R_{80}$ ), and WET.

Thickness (mm)	$R_{80}$ (mm)	WET (mm)
0.25	201.05	0.1
0.5	200.85	0.3
1	200.35	0.8
2	199.25	1.9
4	197.15	4.0
8	192.95	8.2
16	184.75	16.4
32	168.35	32.8
64	135.25	65.9
128	70.55	130.6

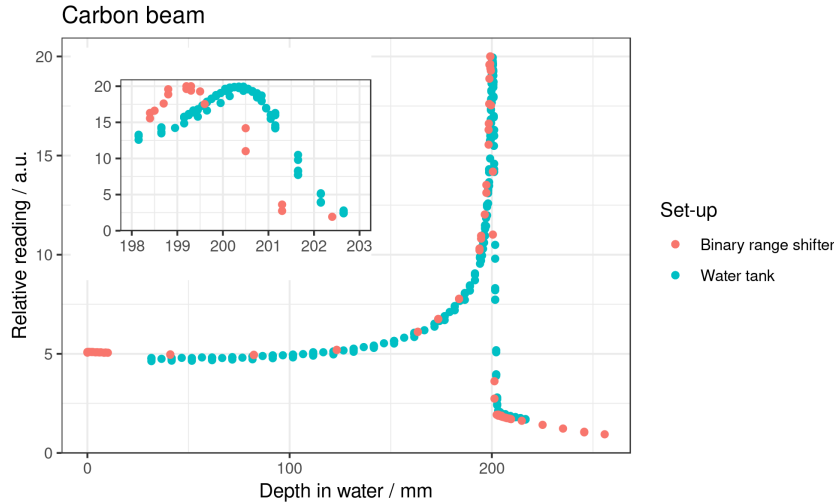


**Figure 17.** Depth-dose profile in water for 326 MeV/n carbon-ion beam and corrected Bragg curve obtained with the binary range shifter.

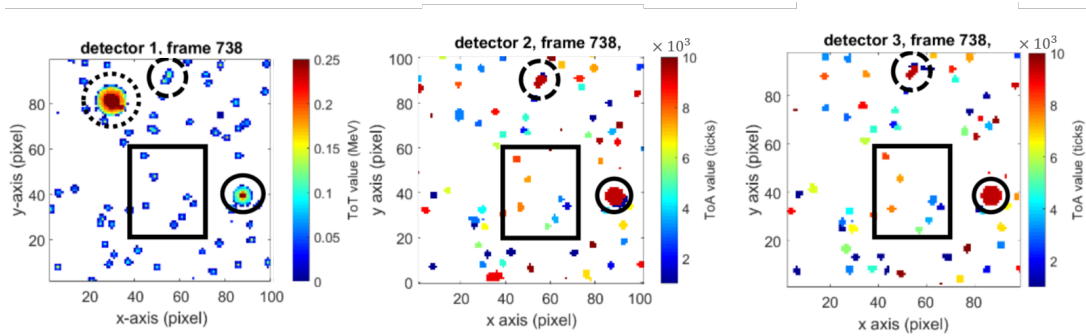


**Figure 18.** Example of raw data signals measured in detector 1, 2, and 3 within a time window of 1 ms. Squares indicate matched signals caused by primary helium ions; full circles indicate three matched signals that are assigned to an impurity ion; the dotted circle indicates a signal on detector 1 that is most likely caused by a recoil nucleus; and the dashed circles indicate overlapping signals of two ions. Signals marked by dotted and dashed circles are rejected from further analysis.

### 235 3.5 Purity of the helium-ion beam

236 The results of the purity analysis of a 173 MeV/n helium-ion beam is presented below.  
 237 Figure 18 shows one data set of a 1 ms-long acquisition, where signals of primary helium  
 238 ions (full square), a signal of a heavier ion due to impurities (full circle), and two types  
 239 of rejected signals (dashed/dotted circles) are marked. The assignment of the signals to  
 240 heavier ions is based on the much higher energy deposition in detector 1 compared to the  
 241 energy deposition of the primary helium ions in that detector. The dotted circle indicates  
 242 a signal that is only measured in detector 1 and is most probably a recoil nucleus, being  
 243 rejected from the further analysis. The dashed circles indicate overlapping signals of two  
 244 ions. The summed energy deposition of the two ions could be mistakenly registered as the  
 245 energy deposition of an impurity ion, and therefore these signals are also rejected.

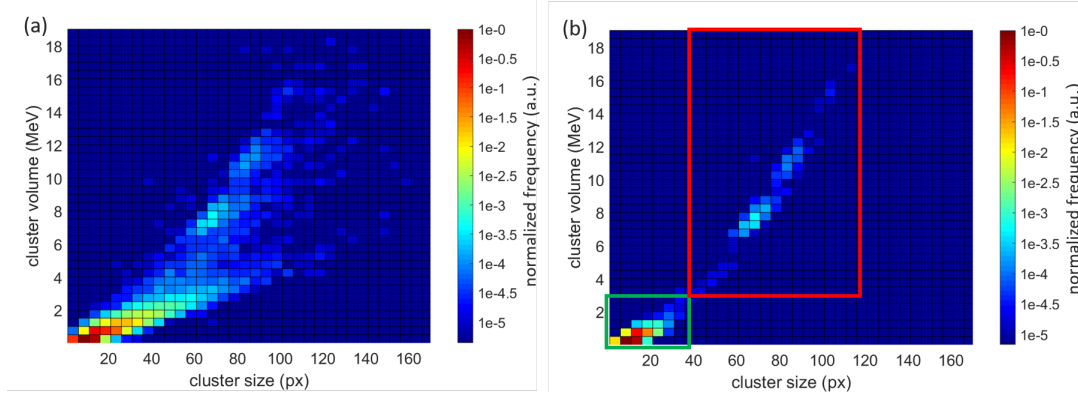


**Figure 19.** Two-dimensional histograms of measured signals, in which they are sorted by their size and their energy deposition. Panel (a): signals measured by detector 1 before the identification and rejection of unwanted background (e.g. recoil nuclei or overlapping signals). Panel (b): signals measured by detector 1 after identification and rejection of unwanted background. The signals in the red square can be related to beam impurities with significantly higher energy depositions than the primary helium ions marked by the green square.

246 Figure 19 shows the comparison of the 2D histograms of measured signals sorted by  
 247 their energy deposition and their cluster size obtained (a) prior and (b) after applying the  
 248 rejection of unwanted background. The background visible in Figure 19(a) would bias the  
 249 determination of the amount of impurities if not suppressed underlining the importance  
 250 of background-suppression. In Figure 19(b) a clear distinction between primary helium  
 251 ions and contamination ions is visible as indicated by the green and red squares. The red  
 252 square includes signals with energy depositions and cluster sizes above 3 MeV and 40 px,  
 253 respectively. These energy depositions > 3 MeV by the contamination ions are significantly  
 254 higher than the energy depositions by the primary helium ions (99.996% of helium ions  
 255 have energy depositions below 2 MeV).

256 Figure 20 presents a three dimensional visualization of the background-suppressed sig-  
 257 nals shown in Figure 19(b). It facilitate the visual identification of the different contributions  
 258 from primary helium ions and beam impurities.

259 The evaluation of the amount of impurity ions (inside the red square in Figures 19(right)  
 260 and 20(a)) with respect to the amount of helium ions (inside the green square) yields

$$\frac{\text{Impurities}}{\text{Helium ions}} = \frac{(0.503 \pm 0.022_{\text{stat}} \pm 0.005_{\text{sys}}) \times 10^3}{(272.91 \pm 0.52_{\text{stat}} \pm 0.38_{\text{sys}}) \times 10^3}$$

261 corresponding to a contamination level of  $0.184 \pm 0.008_{\text{stat}} \pm 0.002_{\text{sys}}\%$  where the uncer-  
 262 tainty is divided into statistical and systematic contributions. The statistical uncertainty  
 263 comprises the count statistics based on the Poisson distribution. The systematic uncer-  
 264 tainty is calculated by varying the vertices of the rectangles in the 2D histogram that are  
 265 used to quantify the amount of primary helium ions and impurity ions (cf. Figures 19 and  
 266 20).

267 A comparison of energy depositions of the impurities with energy depositions of the  
 268 helium ions revealed the two most abundant contaminants to be of atomic numbers in the

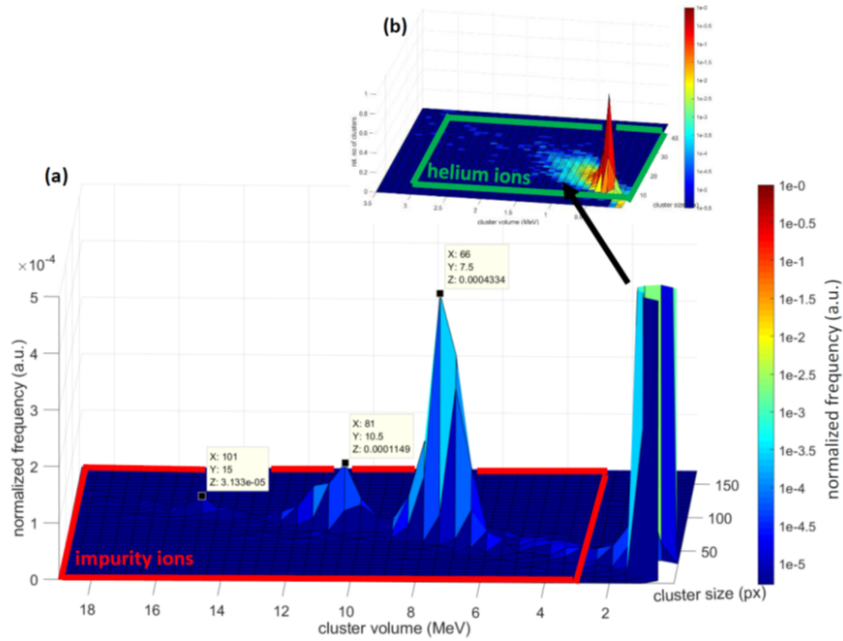


**Figure 20.** Distribution of the relative number of clusters as a function of cluster volume and cluster size. To make the peak heights of the beam impurities visible (about three orders of magnitude lower than the peak for primary helium ions), the scale of the relative number of clusters (vertical axis) in panel (a) was set to  $5 \times 10^{-4}$ . At this scale, the peak of the helium ions is drastically clipped. The inset (b) shows the unclipped distribution of helium clusters.

269 95% confidence intervals (7.77,9.49) and (9.35,11.39). These contaminants are most likely  
 270 oxygen and neon ions, respectively, as these ions can be delivered at the same rigidity as  
 271 the helium ions. Besides, neon is known to be a likely contaminant as it is hard to remove  
 272 all the neon from the helium supply gas.

## 273 4 Conclusions

274 Measurements of reference dosimetry comparing ionization chambers and electrometers  
 275 from NSRL and calibrated complementary devices were performed for proton and carbon ion  
 276 beams. The dose response of the monitor chamber used to cut-off the irradiation indicates  
 277 a highly stable beam. The dose response of the chamber EGG600 was, on average, 2.5%  
 278 higher than the requested dose. Relative deviations of the order of 6% on the measured  
 279 dose was observed across chambers, while the choice of readout device may result in relative  
 280 differences of measured dose up to 4%. Significant differences between the response to  
 281 proton and carbon-ion beams are observed depending on the particular ionization chamber.  
 282 Lateral dose profile measurements in air in the central  $10 \times 10 \text{ cm}^2$  region showed large  
 283 dependence of the chamber response on the position in the field for the irradiation with  
 284 protons. Conversely, for the irradiation with carbon ions, the irradiation field is more  
 285 homogeneous with small dose variations. However, more data are needed to quantify this  
 286 variation and obtain an uncertainty estimate. Regarding depth-dose measurements, results

287 indicate high reproducibility with  $R_{80}$  varying by only 0.2% for proton beams and 0.1% for  
288 carbon-ion beams. The WET values of the layers of the binary range shifter were estimated  
289 and a mean WEPL of 1.025 for HDPE was obtained. Contamination of the helium beam  
290 was evaluated and the presence of ions heavier than helium is less than 0.2%.

## 291 Acknowledgments

292 We would like to thank NIH for the financial support. The support from PTW/PTW US, in  
293 special, Axel Hoffmann, with the logistic of the equipment from DKFZ is highly appreciated.  
294 The work at NSRL is supported by NASA (Contract No. T570X) and performed under the  
295 United State Department of Energy Contract No. DE-AC02-98CH10886.

## 296 References

- 297 [1] J. Miller and C. Zeitlin, *Twenty years of space radiation physics at the BNL AGS and NASA*  
298 *Space Radiation Laboratory*, *Life Sciences in Space Research* **9** (2016) 12–18.
- 299 [2] C. L. Tessa, M. Sivertz, I.-H. Chiang, D. Lowenstein and A. Rusek, *Overview of the NASA*  
300 *space radiation laboratory*, *Life Sciences in Space Research* **11** (2016) 18–23.
- 301 [3] K. D. Held, E. A. Blakely, M. D. Story and D. I. Lowenstein, *Use of the NASA Space*  
302 *Radiation Laboratory at Brookhaven National Laboratory to Conduct Charged Particle*  
303 *Radiobiology Studies Relevant to Ion Therapy*, *Radiation Research* **185** (2016) 563–567.
- 304 [4] M. Durante, H. Paganetti, A. Pompos, S. F. Kry, X. Wu and D. R. Grosshans, *Report of a*  
305 *National Cancer Institute special panel: Characterization of the physical parameters of particle*  
306 *beams for biological research*, *Medical Physics* **46** (2019) e37–e52.